

Structural Evolution of Atomically Thin 1T'-MoTe₂ Alloyed in Chalcogen Atmosphere

Tao Xu, Shouheng Li, Aolin Li, Yue Yu, Hui Zhang, Ping Hu, Wenzhe Zhou, Liping Sheng, Tian Jiang, Haifeng Cheng, Xiang'ai Cheng, Fangping Ouyang,* Jin Zhang,* and Shanshan Wang*

Alloying is widely applied to tailor properties of 2D materials. Herein, a space-confined chemical vapor deposition (CVD) strategy to homogeneously grow 100 μm -sized monolayer 1T'-MoTe₂ in batches is developed. Aberration-corrected annular dark-field scanning transmission electron microscopy combined with density functional theory calculations is applied to investigate the atomic structural alteration of 1T'-MoTe₂ alloyed with sulfur. 1T'-to-2H phase transition is observed, triggered by both thermodynamic (stability improvement) and kinetic (phase transition barrier reduction) reasons. The alloying degrees of MoS₂xTe_{2(1-x)} grown at different temperatures display homophilic and random configurations, respectively, providing a feasible approach to tailor the atomic mixture of the alloying elements. The intralayer reconstruction and the interlayer displacement take place as defect concentration increases at elevated alloying temperatures. In contrast, 1T'-MoTe₂ displays high susceptibility in the presence of oxygen. An encapsulation method is developed using CVD-grown monolayer MoS₂, extending the lifetime of monolayer tellurides from several minutes to at least 24 h. These results gain fundamental insights into the structural change in both the beneficial (sulfurization) and detrimental (oxidation) alloying processes of atomically thin 1T'-MoTe₂ and provide a new degree of freedom for the controllable growth of 2D alloys (i.e., tailoring the alloying degree).

1. Introduction


Alloying has been widely used to tailor material's properties. Metals, such as steels, are fabricated by adding carbon or chromium into the iron matrix to improve the strength and corrosion resistance.^[1] Semiconductors also apply this strategy to produce Al_xGa_{1-x}As, In_xGa_{1-x}N, and Hg_xCd_{1-x}Te for bandgap-tunable electronic and photonic devices.^[2-4] Recently, tremendous efforts have been devoted to preparing 2D transition metal dichalcogenide (TMD) alloys, which adopt atomic thickness, diverse electronic structures, and show great potential in nano-electronics, flexible devices, and energy-harvesting applications.^[5-14] Janus TMD monolayer alloys having different chalcogen atoms situating at the top and bottom atomic planes separately break the out-of-plane mirror symmetry, thus generating vertical dipoles and enabling spin manipulation.^[15,16] High-entropy 2D TMD alloys combining multiple metal components in near-equiatom concentrations exhibit outstanding electrochemical performance.^[17]

Ternary TMD alloys involving two types of chalcogen elements randomly distributed are one of the most intensively studied

T. Xu, T. Jiang, X. Cheng
College of Advanced Interdisciplinary Studies
National University of Defense Technology
Changsha 410073, P. R. China

S. Li, H. Zhang, H. Cheng, S. Wang
Science and Technology on Advanced Ceramic Fibers and Composites
Laboratory
College of Aerospace Science and Engineering
National University of Defense Technology
Changsha 410000, P. R. China
E-mail: wangshanshan08@nudt.edu.cn

A. Li
Powder Metallurgy Research Institute
Central South University
Changsha 410073, P. R. China

 The ORCID identification number(s) for the author(s) of this article can be found under <https://doi.org/10.1002/sstr.202200025>.

DOI: 10.1002/sstr.202200025

Y. Yu, J. Zhang
Center for Nanochemistry
Beijing Science and Engineering Center for Nanocarbons
Beijing National Laboratory for Molecular Sciences
College of Chemistry and Molecular Engineering
Peking University
Beijing 100871, P. R. China
E-mail: jinzhang@pku.edu.cn

P. Hu, L. Sheng
National Local Joint Engineering Laboratory for New Petro-chemical
Materials and Fine Utilization of Resources
College of Chemistry and Chemical Engineering
Hunan Normal University
Changsha 410081, P. R. China

W. Zhou, F. Ouyang
School of Physics and Electronics
Central South University
Changsha 410083, P. R. China
E-mail: oyfp@csu.edu.cn

systems.^[8,18–27] Taking group-VIB 2D TMD alloys for instance, they can generally be categorized into three groups based on their phases and 2D structural integrity (**Figure 1**). The first group contains S and Se as chalcogen atoms with typical examples of $\text{MoS}_{2x}\text{Se}_{2(1-x)}$ and $\text{WS}_{2x}\text{Se}_{2(1-x)}$ monolayers.^[8,19–21] These 2D alloys predominantly remain the energetically favorable layered 2H phase at the full range of the compositional space (middle panel of Figure 1). Their atomically thin structural integrity can be maintained during the alloying process with a tunable bandgap (approximately several hundred millielectron volts) by altering the ratio between S and Se.^[8,22,23] When Te is involved, the phase diagram as a function of the chalcogen concentration changes.^[24,25] We assign this alloying scenario to the second group (right panel of Figure 1). Alloys such as $\text{WSe}_x\text{Te}_{2(1-x)}$ monolayers display 2H-to-1T' phase transition as the composition changes because the energy difference between the two phases for transition metal tellurides is small.^[26,27] As the two polymorphs exhibit semiconducting and semimetallic properties, respectively, Te-contained 2D TMD alloys show a wide-range electronic structure alteration from semiconductor to metal with a tunable chemical composition. The 2D structure is preserved during the phase transition due to the layered configuration of both hexagonal 2H and monoclinic 1T' phases. Alloying between 1T'- MoTe_2 and oxygen (O) is referred as the third group (left panel of Figure 1), which can be the source of catalytic performance improvement reported by previous literatures,^[28] yet in most cases, it is considered as an undesirable process. 2D structural integrity is degraded by oxidation due to the nonlayered configuration of most transition metal oxides.^[29–31] This phenomenon is prominent in transition metal tellurides due to weak metal–tellurium bonds. Therefore, strategies to prohibit

this alloying process were developed including coating various encapsulation layers ranging from polymers to 2D materials like graphene and h-BN.^[32–34]

Given that mixing different chalcogen species to TMD monolayers leads to diverse phases and properties, unveiling the multiscale structural evolution in the alloying process from micrometer to atomic level is of great significance for design, preparation, and exotic property discovery of 2D TMD alloys. Limited investigations have been reported so far especially for the Te-based atomically thin alloys. Yu et al. demonstrated the 2H-1T' phase transition in $\text{WSe}_{2x}\text{Te}_{2(1-x)}$ monolayer exfoliated from chemical vapor transport (CVT)-grown single crystals as the Te concentration increases and found the coexistence of the two phases when Te accounted for 50% of chalcogen atoms.^[26] Yun et al. tellurized MoS_2 and WS_2 monolayers by vapor phase reaction and reported similar phase transition by Raman spectroscopy.^[35] Lin et al. disclosed anisotropic arrangement of chalcogen atoms in 1T'- $\text{MoSe}_{2x}\text{Te}_{2(1-x)}$ by scanning transmission electron microscopy (STEM) and attributed the reason to inequivalent bonding in this low-symmetry phase.^[27] However, a systematic study tracking the structural evolution of atomically thin 1T'- MoTe_2 in different chalcogen atmospheres via both spectroscopy and high-resolution imaging is lacking presumably due to the challenge of both producing high-quality MoTe_2 atomic layers and conducting cutting-edge electron microscopy experiments. Detailed intralayer and interlayer configurations and potential segregations at atomic scale in the Te-based alloys remain elusive, which hinders the understanding and manipulation of physicochemical properties of 2D TMD alloys.

In this work, we design a space-confined CVD approach to enable the batch production of uniform 1T'- MoTe_2 monolayers with lateral sizes of 80–100 μm by varying the flow dynamics in the confined gap, establishing material foundation for the alloying study. Atomically thin 1T'- MoTe_2 alloyed with S is subsequently investigated. Subangstrom resolution annular dark field scanning transmission electron microscopy (ADF-STEM) is conducted to uncover the phase transition, atomic substitution, alloying degree, and interlayer registry. The quick structural degradation of 1T'- MoTe_2 by uncontrollable alloying with oxygen in air is subsequently identified by comprehensive characterizations. A swift and clean antioxidation method is developed by encapsulating 1T'- MoTe_2 with CVD-grown monolayer MoS_2 , which can both protect monolayer tellurides and fabricate van der Waals (vdW) 1H- MoS_2 /1T'- MoTe_2 heterostructures in batches. Density functional theory (DFT) calculations are applied to help understand the phase transition mechanism of 1T'- MoTe_2 after alloying with sulfur and the oxidation process.

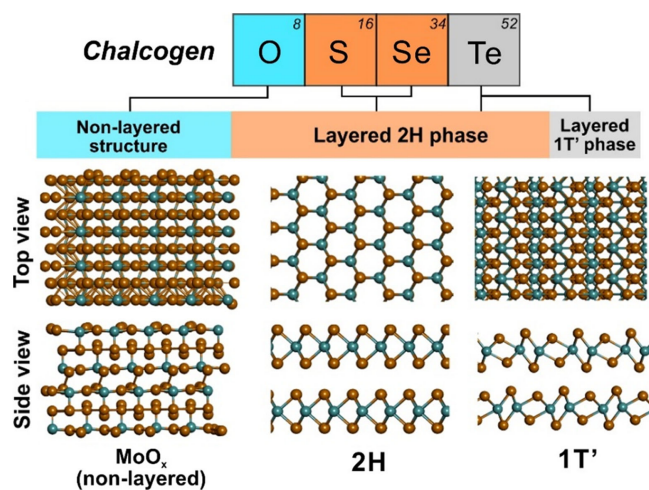


Figure 1. Schematic illustration showing three types of scenarios when 2D TMDs (e.g., group VIB TMDs) are alloyed with different chalcogen elements. Green and orange spheres in the atomic models represent metal and chalcogen atoms, respectively. Type I (middle panel): The incorporation of S and Se atoms leads to the formation of 2H phase TMD alloys with well-maintained 2D structural integrity. Type II (right panel): The involvement of Te also preserves the 2D structure but may trigger the 2H-1T' phase transition as Te concentration increases. Type III (left panel): Alloying with O results in the generation of nonlayered metal oxides, which destroys the 2D structural integrity of TMD atomic layers.

2. Results and Discussion

2.1. Space-Confined CVD Growth of Uniformly Distributed 1T'- MoTe_2 Monolayers

We applied a space-confined CVD method by constructing laminated pairs of substrates to synthesize 1T'- MoTe_2 atomic layers in batches.^[36–40] Five pairs of substrates with face-to-face stacking were vertically arranged in the furnace center, simultaneously generating multiple microreactors with special fluid dynamics

(Figure 2a). Sodium molybdate (Na_2MoO_4) and sodium chloride (NaCl) mixed aqueous solution, serving as the Mo-contained precursor, were uniformly spin coated on the bottom chip of each substrate pair. Tellurium (Te) powder was vaporized upstream and transported to the reaction zone. The preparation was carried out at 750°C under atmospheric pressure with a mixed carrier gas of argon and hydrogen (see Experimental Section).

2D leaf-like MoTe_2 domains with lateral sizes of $80\text{--}100\ \mu\text{m}$ were homogeneously grown on the top SiO_2/Si chip of each substrate pair when the gap size was carefully adjusted to $\approx 24\ \mu\text{m}$ (Figure 2b, S1, Supporting Information). The domain size shrank remarkably with a high nucleation density and inferior spatial/thickness uniformity when the space-confined strategy was not applied (Figure 2c). This method is applicable to various substrates, including a-sapphire, quartz, and graphene, covering materials with different dimensionalities and electronic properties (Figure 2d–e, S2a, Supporting Information). Raman spectra of as-grown samples on different substrates were displayed in Figure 2f. Taking MoTe_2 on SiO_2/Si as an example, characteristic peaks located at $86, 109, 128, 252,$ and $269\ \text{cm}^{-1}$ correspond to A_g vibrational modes, while peaks situated at $102, 162,$ and $188\ \text{cm}^{-1}$ correspond to B_g vibrational modes, manifesting the achievement of the $1\text{T}'$ phase.^[41–43] The thickness of the measured region is single layer as confirmed by the peak position of the A_g mode at $269\ \text{cm}^{-1}$.^[34] The preparation of $1\text{T}'\text{-MoTe}_2$ did not impair the quality of the graphene substrate, as peaks at $1582\ \text{cm}^{-1}$ (G peak) and $2700\ \text{cm}^{-1}$ (2D peak) were well preserved (Figure S2b, Supporting Information).^[37,44]

The mechanism of the space-confined CVD growth of $1\text{T}'\text{-MoTe}_2$ atomic layers was demonstrated in detail in the

supporting information (See Part 2, Supporting Information). In brief, confined space alters the flow state, changing the viscous flow, in which collision between gas molecules dominates, to Knudsen flow, in which collision between gas molecules and tube walls prevails. The viscous-to-Knudsen flow state transition is equivalent to decreasing the chamber pressure, thus shifting the rate-limiting step of the CVD growth from mass transport to surface reaction (Figure 2h). Therefore, the negative impact of spatial inhomogeneity of the precursor vapor in the bulk gas phase will be blocked, ensuring homogenous distribution of atomically thin $1\text{T}'\text{-MoTe}_2$ domains across the substrate. Figure 2g displays the gas flow state (defined by the Knudsen number) and the equivalent pressure as a function of the gap size. Inset shows that, when the gap size is reduced to $23.6\ \mu\text{m}$, the flow state alters to Knudsen flow with a Knudsen number greater than 0.01, which equals to pump the chamber pressure down to $94.6\ \text{Pa}$. Our optimal synthesis result was achieved by constructing a gap size of $\approx 24\ \mu\text{m}$, which is at the critical point of the viscous-to-Knudsen flow state transition.

2.2. Structural Evolution of $1\text{T}'\text{-MoTe}_2$ Atomic Layers Alloyed in Sulfur Atmosphere

We first carried out experiments to investigate the configuration change of $1\text{T}'\text{-MoTe}_2$ after alloying with sulfur. The fresh $1\text{T}'\text{-MoTe}_2$ sample was heated in S vapor at 250°C for 5 min (see Experimental Section). The decreased chemical activity of S with respect to O and the layered structure of MoS_2 preserve the 2D structural integrity of sulfurized $1\text{T}'\text{-MoTe}_2$ and provide opportunities to track the alloy configuration down to

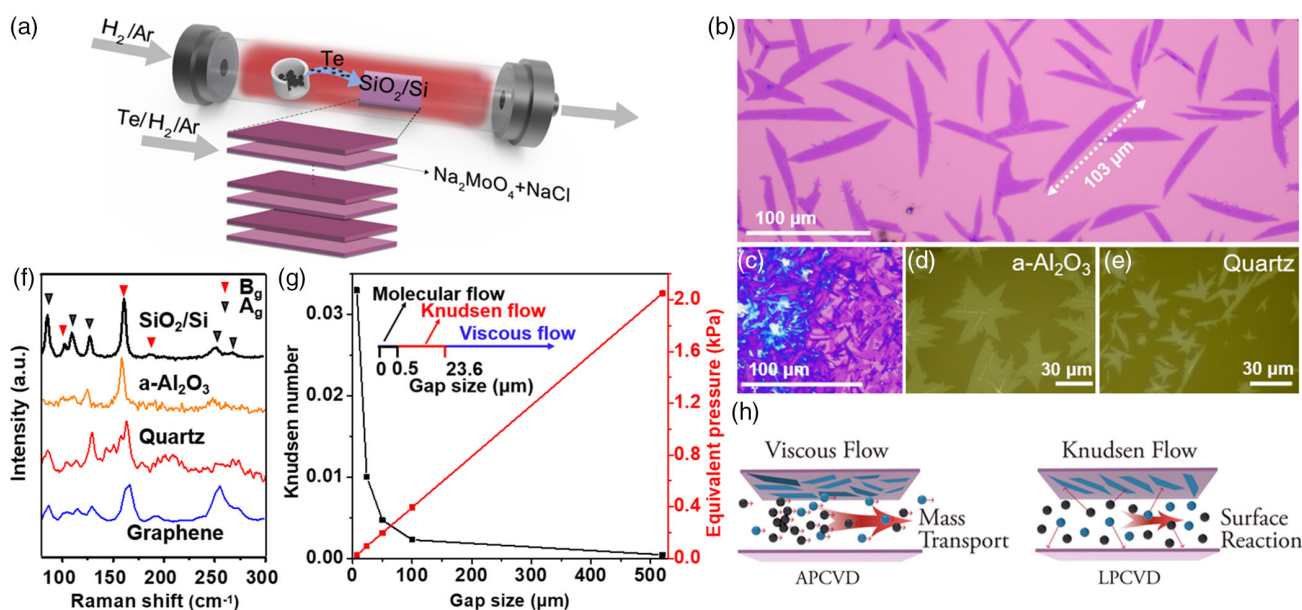


Figure 2. a) Schematic illustration of the space-confined CVD setup for the batch growth of monolayer $1\text{T}'\text{-MoTe}_2$. b) Optical image of $1\text{T}'\text{-MoTe}_2$ monolayers on the SiO_2/Si substrate. c) Optical image of $1\text{T}'\text{-MoTe}_2$ grown without space confinement. d,e) Optical images showing space-confined CVD preparation of $1\text{T}'\text{-MoTe}_2$ on a-sapphire and quartz substrates, respectively. f) Raman spectra of as-grown $1\text{T}'\text{-MoTe}_2$ on various substrates. g) Plot displaying the Knudsen number and the equivalent pressure in the confined space as a function of the gap size, respectively. Inset depicts the gap size ranges corresponding to viscous flow, Knudsen flow, and molecular flow, respectively. h) Schematics demonstrating the mechanism of the uniform growth of $1\text{T}'\text{-MoTe}_2$ within the confined space.

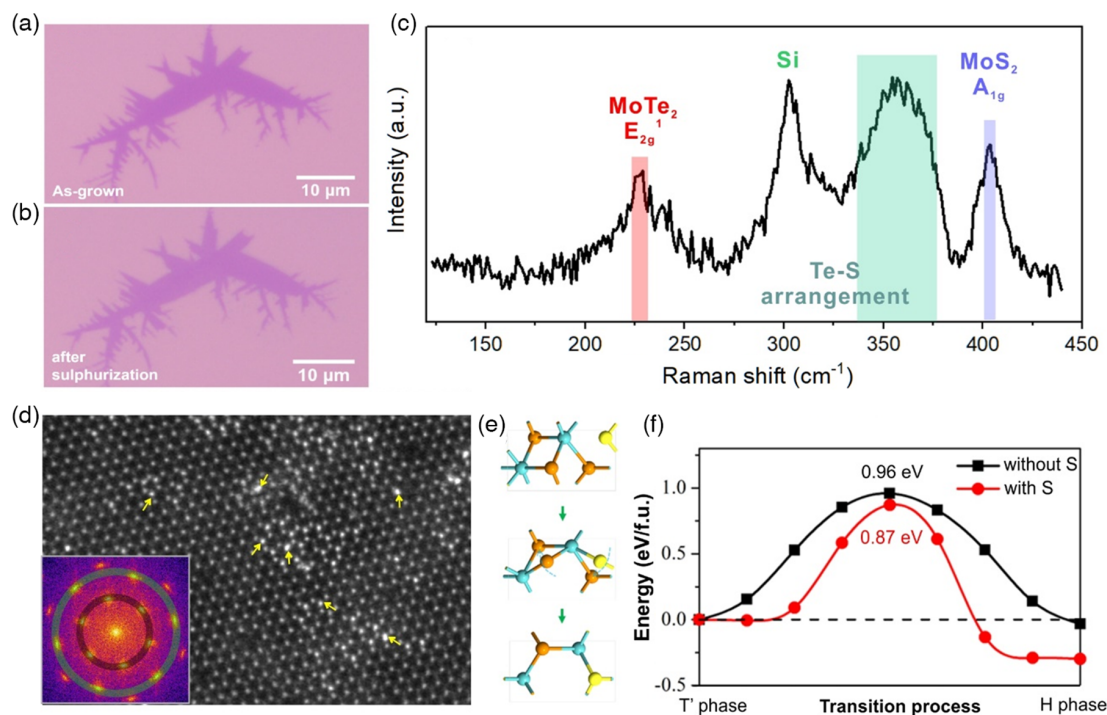


Figure 3. a,b) Optical images of monolayer 1T'-MoTe₂ before and after alloying with S at 250 °C. c) Raman spectrum of the sulfurized monolayer MoTe₂. d) ADF-STEM image of the sulfurized MoTe₂ monolayer. Inset shows the corresponding FFT image. Yellow arrows indicate some Te atoms in the lattice with high brightness. e) DFT-calculated model showing the atomic movement of 1T'-to-2H' phase transition when 1T'-MoTe₂ is alloyed with S. Green, orange, and yellow spheres represent Mo, Te, and S atoms, respectively. f) Energy profiles of the 1T'-2H phase transition for 1T'-MoTe₂ with (red) and without (black) sulfur substitution.

the single-atom level. **Figure 3a,b** shows the optical images of monolayer 1T'-MoTe₂ layers before and after sulfurization. The optical contrast of the material became lighter after sulfurization, which proves that the reaction has taken place and indicates the alteration of material permittivity. **Figure 3c** displays the Raman spectrum of the sulfurized 1T'-MoTe₂. The peak located at $\approx 405\text{ cm}^{-1}$ can be assigned to the out-of-plane vibration of MoS₂, indicating the formation of 2H-MoS₂.^[45] The emergence of a prominent peak at $\approx 230\text{ cm}^{-1}$ can be assigned to the E_{2g}^1 mode in 2H-MoS₂, which has also been observed in the tellurized monolayer 2H-MoS₂.^[35,46,47] The results indicate the 1T'-2H phase transition in the sulfurization process with an increased level of structural disorder. In addition, a broad peak situating at $\approx 355\text{ cm}^{-1}$ highlighted by the green column in **Figure 3c** represents the complicated atomic arrangement of Te and S species in the sulfurized MoTe₂.^[35] Two potential configurations are present. One is called the Janus structure, where S and Te in the alloy are in separated atomic layers, while the other structure is the random mixture of Te and S species in the sulfurized MoTe₂. Based on the previous calculated Raman spectrum in which peaks corresponding to these two structures are located at 339.9 and 352.9 cm^{-1} , respectively, both two structures could be present in our sample.^[35] However, precise assignment may require further work.

Figure 3d displays the ADF-STEM image revealing the phase transition and the atomic configuration of the sulfurized 1T'-MoTe₂. The original low-symmetry monoclinic phase of

1T'-MoTe₂ was altered to the hexagonal 2H phase alloy. Inset shows the fast Fourier transform (FFT) image of **Figure 3d**, in which reflexes corresponding to the zigzag and armchair lattice directions are labeled by the inner and outer circles, respectively, manifesting the hexagonal crystal structure. The ADF-STEM image exhibits spots with different brightness. The bright spots, marked by yellow arrows, correspond to the atomic sites that involve heavy Te atoms, as the intensity of the ADF-STEM images is positively correlated with the atomic number of the column. The less bright and dim spots correspond to the Mo and 2S sites, respectively, indicating the formation of the monolayer alloy involving Mo, S, and Te species.

To understand the sulfur-mediated 1T'-to-2H transition in MoTe₂, we analyzed the phase transition process using the nudged elastic band (NEB) method in first-principles calculations. As shown in **Figure 3e,f**, the phase transition barrier from 1T' to 2H phase of the pristine monolayer MoTe₂ is 0.96 eV f.u.⁻¹ and the energy difference is $-0.03\text{ eV f.u.}^{-1}$ between the 1T' and the 2H phase, in line with the literature.^[48] However, when some Te atoms are substituted by S atoms (25% in this case), the transition barrier is reduced to 0.87 eV f.u.⁻¹ and the energy difference is decreased to $-0.30\text{ eV f.u.}^{-1}$ between the 1T' and the 2H phase. These results suggest that sulfur substitution in 1T'-MoTe₂ plays a significant role in both improving the 1T'-to-2H phase transition speed and enhancing the stability of the 2D MoS₂_xTe_{2(1-x)} alloy. Notably, the phase transition pathways can be affected by point defects, but they do not change the beneficial effect of

sulfur substitution on the 1T'-to-2H phase transition (Figure S3, S4, Supporting Information).

The detailed structure at each atomic column in the monolayer 2H-MoS_{2x}Te_{2(1-x)} alloy was carefully examined. Figure 4a shows a region of the monolayer alloy. A typical area corresponding to the yellow-boxed region in panel (a) was zoomed in, where atoms with mainly four levels of brightness were seen. The intensity variation can be visualized more clearly using color rendering, as displayed in Figure 4c. With the help of atomic model construction and the ADF-STEM image simulation, it was determined that the brightest atomic columns with an intensity of ≈80–200 arbitrary units (a.u.) correspond to a Mo+Te structure, representing a Te atom adsorbed on the surface of a Mo atom, as marked by the red dashed circles in panel (c) and (d), respectively. The second-bright columns locate at the bichalcogen (X₂) sites with an intensity of ≈140 a.u., which can be assigned to the vertically stacked S + Te structure, as marked by the black dashed circles in panel (c) and (d). The third-bright columns correspond to the normal single Mo sites and the dimmest columns are double-stacked S sites. The deduction can be verified by Figure 4e, which is the ADF-STEM image simulation based on the model in panel (d). The simulated image is consistent with the experimental one in panel (b). Figure 4f,g shows intensity line profiles taken along the yellow and cyan boxed regions in both the experimental (panel b) and the simulated (panel e) ADF-STEM images, respectively, further proving our analysis of the atomic distribution of different elements in the 2D alloy quantitatively.

We also counted the intensity distribution of the atoms in the image (Figure 4h). Four typical structures at the Mo sites can be discriminated based on the intensity histogram at the top panel in Figure 4h: 1) a single Mo atom with an intensity of ≈100 a.u.,

2) a single Te atom with an intensity of ≈115 a.u., 3) a Te atom adsorbed on a Mo atom (Mo+Te), and 4) double-stacked Te atoms (2Te). The last two structures are few and they display similar intensity ranging from 170 to 200 a.u. due to close atomic numbers between Te and Mo. It is worth noting that, distinct from many other TMD alloys in which nonmetal atoms cannot occupy metal sites,^[9,18–20,22,25,26,35,49] the chalcogen atom Te can situate at the Mo sites either on the surface as adsorbents or in lattice as substitution of Mo. The phenomena may be derived from 1) an increased level of metallicity of Te compared with other chalcogen elements, such as Se and S, making it easier to incorporate into the metal sites; and 2) the 1T'-2H phase transition during alloying that involves prominent atomic displacement and reconstruction as well as defects, offering opportunities to generate and stabilize the anomalous structures. The bottom panel in Figure 4h exhibits the intensity distribution at X₂ sites. Different intensity regions can be assigned to single S sites, double S sites, single Te sites, S plus a Te site (S + Te), and double Te sites, respectively, verifying diverse substitutional modes between S and Te.

We then investigated the atomic distribution of Te and S in the monolayer MoS_{2x}Te_{2(1-x)} alloy, which can be quantitatively evaluated by a parameter, denoted as the alloying degree (*J*).^[50,51] Mathematically, the alloying degree of one type of element, for example, tellurium atoms, in monolayer MoS_{2x}Te_{2(1-x)} can be expressed as

$$J(\text{Te}) = P(\text{observed})/P(\text{random}) \times 100\% \quad (1)$$

in which *P*(observed) represents the ratio of the averaged coordination number of the S atoms around a Te atom to the total

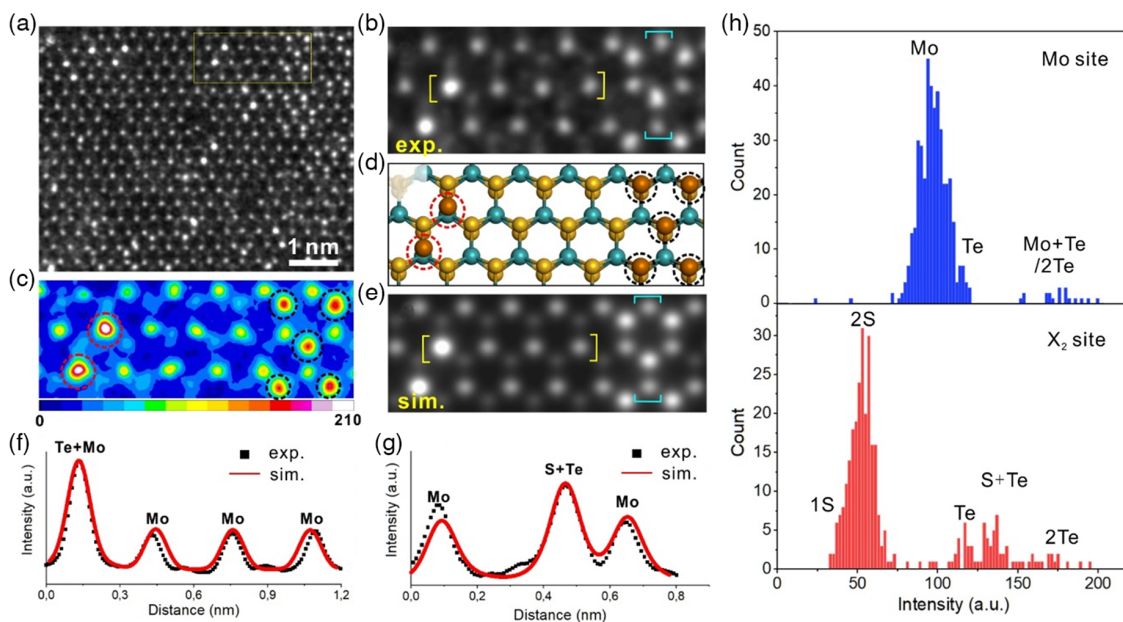


Figure 4. a) ADF-STEM image of the MoS_{2x}Te_{2(1-x)} monolayer. b) Zoomed-in ADF-STEM image corresponding to the yellow-boxed region in panel (a). c) Color-rendered ADF-STEM image of panel (b). d) Atomic model based on panel (b). Green, yellow, and brown spheres represent Mo, S, and Te atoms, respectively. e) Image simulation based on the model in panel (d). f) Intensity line profiles taken along the regions in the yellow brackets from left to right in panels (b) and (e), respectively. g) Intensity line profiles taken along the regions in the cyan brackets from top to bottom in panels (b) and (e), respectively. h) Intensity histograms of the Mo sites and the bichalcogen (X₂) sites in panel (a).

coordination number of a Te atom (six, if no vacancy exists) in the observation area. $P(\text{random})$ is defined as the atomic ratio of the S atoms in the examined region (See Part 3, Supporting Information). We ignored Mo sites in this study. Only S and Te atoms in the chalcogen sites were considered. Te atoms adsorbed at the Mo sites were neglected because they are very few. The total coordination number of a chalcogen atom is considered as six, as we do not discriminate chalcogen atoms at the top and bottom atomic planes in the monolayer alloy.

The variation of the alloying degree can significantly influence the atomic distribution of different elements, leading to various modes of phase separation or segregation and altering materials properties, such as catalytic performance.^[52] Taking Figure 5a as an instance, the number of Te atoms accounts for half of the total number of the chalcogen sites in this scenario, yielding $P(\text{random}) = 50\%$. However, if examining the average number of S atoms coordinated around each Te atom down to single-atom level, it was found that S atoms only aggregate with S atoms and Te agglomerate with Te atoms, suggesting that there is no S atom surrounding the Te atom, yielding $P(\text{observed}) = 0$. The heterostructure interface is neglected here, as the area of MoS_2 and MoTe_2 on both sides is assumed to be infinite. Therefore, J equals to 0, indicating a complete segregation between S and Te elements at atomic scale, which corresponds to an in-plane heterostructure. When $J < 100\%$, S(Te) atoms prefer to attract S(Te) atoms as their neighbors, leading to the formation of discrete S(Te) clusters in the alloy matrix (Figure 5b). Such type of atomic distribution is called homophilic structure. When $J = 100\%$, no preference is seen for the arrangement of

S and Te atoms. The alloy is a randomly mixed solid solution (Figure 5c). Finally, if $J > 100\%$, S atoms are prone to gather Te atoms around and Te atoms prefer to aggregate with S atoms. In this scenario, the alloy exhibits heterophilic configuration. Figure 5d depicts a typical geometric distribution of Te atoms in the $\text{MoS}_{2x}\text{Te}_{2(1-x)}$ alloy that adopts heterophilic configuration. Te atoms are linearly arranged, making the length of S–Te boundary as long as possible.

We analyzed the alloying degree of the $\text{MoS}_{2x}\text{Te}_{2(1-x)}$ alloy, which was achieved by the sulfurization of $1\text{T}'\text{-MoTe}_2$ at 250°C (Figure 5e). S and Te atoms are labeled in disparate colors based on their numbers of heteroatoms in the neighboring sites (Figure 5f). Spots in red, yellow, cyan, green, pink, orange, and blue represent S atoms having zero, one, two, three, four, five, and six Te atoms coordinated as the closest neighbors, respectively. Similarly, squares represent Te atoms with distinct colors indicating different numbers of the surrounding S atoms. It was found that the alloying degrees of S and Te atoms in this area are 65.4% and 67.2%, respectively. Another selected region of the $\text{MoS}_{2x}\text{Te}_{2(1-x)}$ alloy gave similar results, yielding 72.3% and 70.7% for $J(\text{S})$ and $J(\text{Te})$, respectively (Figure S5a,b, Supporting Information). These alloying degree values, as recorded in the plot of Figure 5i, are less than 100%, indicating the formation of the homophilic structure for $\text{MoS}_{2x}\text{Te}_{2(1-x)}$ with an alloying temperature of 250°C . Interestingly, this result is distinctive from previously reported TMD alloys that have a random mixture of chalcogen atoms.^[19,51] The reason may originate from the low sulfurization temperature (250°C) of $1\text{T}'\text{-MoTe}_2$, making enthalpy rather than entropy the dominant factor of Gibbs free

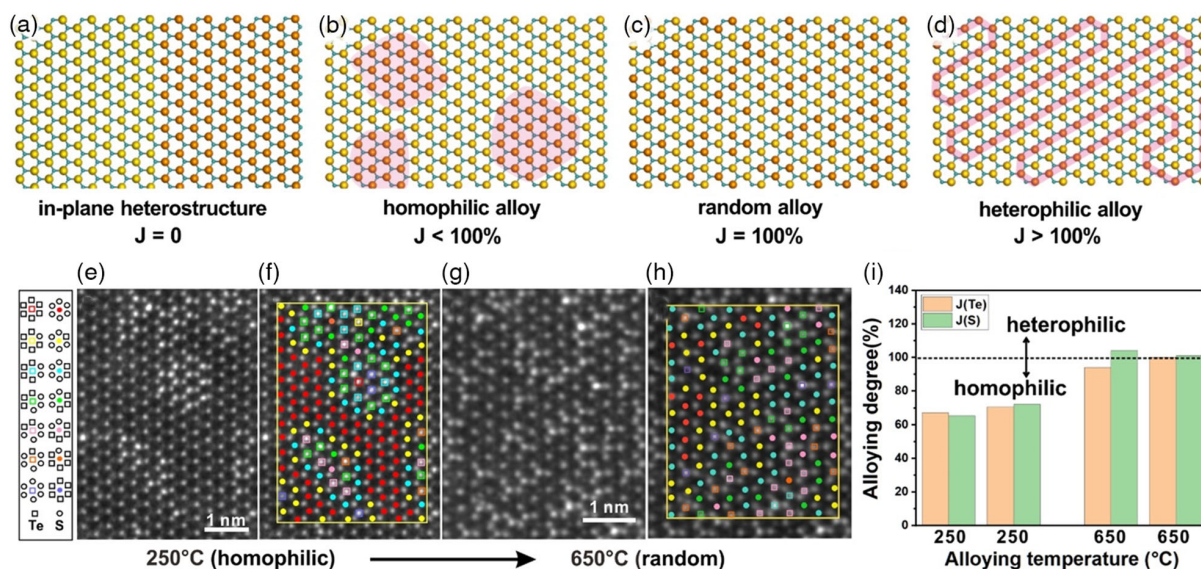


Figure 5. a–d) Schematics showing four representative types of atomic distributions of Te and S atoms with different values of the alloying degree. Large yellow and orange spheres indicate S and Te atoms, respectively, while small green spheres represent Mo atoms. Te clusters and Te atomic lines are highlighted by pink masks in panel (b) and (d) to highlight the geometric feature of homophilic and heterophilic alloys, respectively. e,g) ADF-STEM images of monolayer $\text{MoS}_{2x}\text{Te}_{2(1-x)}$ alloyed at 250 and 650°C , respectively. f,h) ADF-STEM images correspond to panel (e) and (g), respectively, in which S and Te atoms with different numbers of heteroatomic coordination sites are labeled in different colors. Spots represent S atoms, while squares represent Te atoms. Spots in red, yellow, cyan, green, pink, orange, and blue represent S atoms having zero, one, two, three, four, five, and six Te atoms coordinated as the closest neighbors, respectively. Squares in red, yellow, cyan, green, pink, orange, and blue represent Te atoms having zero, one, two, three, four, five, and six S atoms coordinated as the closest neighbors, respectively. i) Histogram showing the alloying degrees of $J(\text{Te})$ and $J(\text{S})$ counted at four different regions of $\text{MoS}_{2x}\text{Te}_{2(1-x)}$ alloyed at 250 and 650°C , respectively.

energy. Therefore, Te and S atoms prefer not to mix thoroughly due to insufficient motivation to overcome the diffusion barrier in the basal plane lattice, leading to phase segregation.

To partially verify the temperature dependence on the alloying degree and its adjustability, we synthesized another $\text{MoS}_{2x}\text{Te}_{2(1-x)}$ monolayer under a high alloying temperature of 650 °C by tellurizing monolayer MoS_2 (Figure 5g,h, see Experimental Section). The reason why we did not grow $\text{MoS}_{2x}\text{Te}_{2(1-x)}$ by sulfurizing $1\text{T}'\text{-MoTe}_2$ is due to the low chemical stability of $1\text{T}'\text{-MoTe}_2$ at high temperature. The alloying degree of S and Te atoms in this case is 104.2% and 94.0%, respectively. Another region of the same sample exhibits $J(\text{S}) = 101.3\%$ and $J(\text{Te}) = 100.3\%$, respectively (Figure S5c,d, Supporting Information). All the values are close to 100%, suggesting the random mixture of Te and S elements when the alloying temperature was increased to 650 °C (Figure 5i). In addition, the chemical formulas of the monolayer TMD alloys achieved at 250 and 650 °C are $\text{MoS}_{1.72}\text{Te}_{0.24}$ and $\text{MoS}_{1.62}\text{Te}_{0.33}$ (See Part 4, Supporting Information), respectively. The slight deviation of the atomic ratio between Mo and chalcogen sites from 1:2 is due to the presence of a small number of vacancies in the alloy. These results give insights into the atomic distribution of different elements in the TMD alloy and suggest a new degree of freedom to tailor the 2D alloy structure, apart from the conventional composition aspect.

The atomic structure of 2D $\text{MoS}_{2x}\text{Te}_{2(1-x)}$ as a function of the alloying temperature has also been studied. When the sulfurization temperature was enhanced from 250 to 350 °C, the atomic ratio of Te decreased when an increasing number of holes (average size of $\approx 1 \text{ nm}^2$) opened up in the membrane due to the chemical instability of monolayer $1\text{T}'\text{-MoTe}_2$ (Figure 6a). Even though most areas of MoTe_2 have been changed to the 2H phase after sulphurization, there still remain small regions of $1\text{T}'$ phase, which provide evidence for the monoclinic structure of $1\text{T}'\text{-MoTe}_2$ before alloying (Figure 6b). Figure 6c shows the zoomed-in image of the $1\text{T}'\text{-2H}$ junction region in Figure 6b. The cyan-shaded region adopts the $1\text{T}'$ phase with alternating

chain-like structures, which is disparate from the hexagonal lattice (2H phase) on the right, indicating its low structure symmetry. Inset proposes a potential phase junction configuration between 2H and $1\text{T}'$ based on the atomic structure in the red-boxed region. Despite the 2H and $1\text{T}'$ phases, we also observed stripe-like configuration in the monolayer alloy (Figure 6d), as shaded in cyan. It was generated by the transversal displacement of chalcogen atoms along the armchair direction by $a/2\sqrt{3}$ (a is the lattice constant of the 2H phase lattice), as indicated by the red arrows in Figure 6e, leading the original hexagonal lattice to become the rectangle configuration (Figure 6f). Figure 6g shows the multislice ADF-STEM image simulation based on the model in panel (f), agreeing well with the experimental image in panel (d). The generation of the strip-like lattice structure may be derived from the surrounding defects, such as holes and vacancies, that motivate the lattice distortion locally.^[53] The in-plane strain may also contribute to the relatively large radius difference between S and Te atoms. These results show the polymorphism and structural diversity in the sulphurized $1\text{T}'\text{-MoTe}_2$ monolayers.

When the sulfurization temperature was increased to 550 °C, almost all monolayer regions were decomposed. Only a small quantity of bilayer $\text{MoS}_{2x}\text{Te}_{2(1-x)}$ can be observed due to the existence of very few $1\text{T}'\text{-MoTe}_2$ bilayer regions in the CVD-prepared sample. It provides opportunities to examine the interlayer stacking registries at atomic scale, which is closely correlated with physical and chemical properties of 2D materials, including band structures, catalytical performances, mechanical properties, magnetism, etc.^[54–60] Figure 7a shows an ADF-STEM image, where regions that are not shaded in yellow are bilayers. Various types of Moiré patterns were displayed in bilayer areas, which may be triggered by the defect generation in the phase transformation process that motivates interlayer displacement.^[61] Four typical kinds of bilayer structures are selected, as shown in Figure 7b–e, with their corresponding atomic models and image simulations displayed in Figure 7f–i,j–m, respectively. The stacking sequences of these bilayer regions can be denoted as AA',

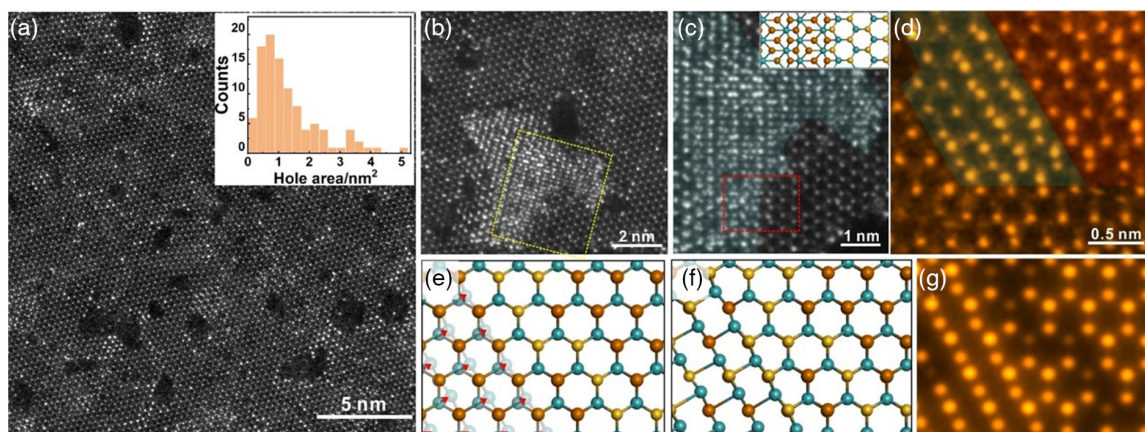


Figure 6. a) ADF-STEM image of $\text{MoS}_{2x}\text{Te}_{2(1-x)}$ monolayer with an alloying temperature of 350 °C. Inset shows the histogram displaying the hole area distribution. b) ADF-STEM image showing a region containing 2H and $1\text{T}'$ phases simultaneously. c) Zoomed-in ADF-STEM image corresponding to the yellow-boxed region in panel (b). Inset shows the atomic model schematically depicting the potential 2H- $1\text{T}'$ phase junction structure. d) High-magnification ADF-STEM image showing a squared lattice structure, as shaded in cyan. e, f) Models showing the potential atomic movement from the hexagonal to the squared lattice. g) Multislice ADF-STEM image simulation based on the model in panel (f).

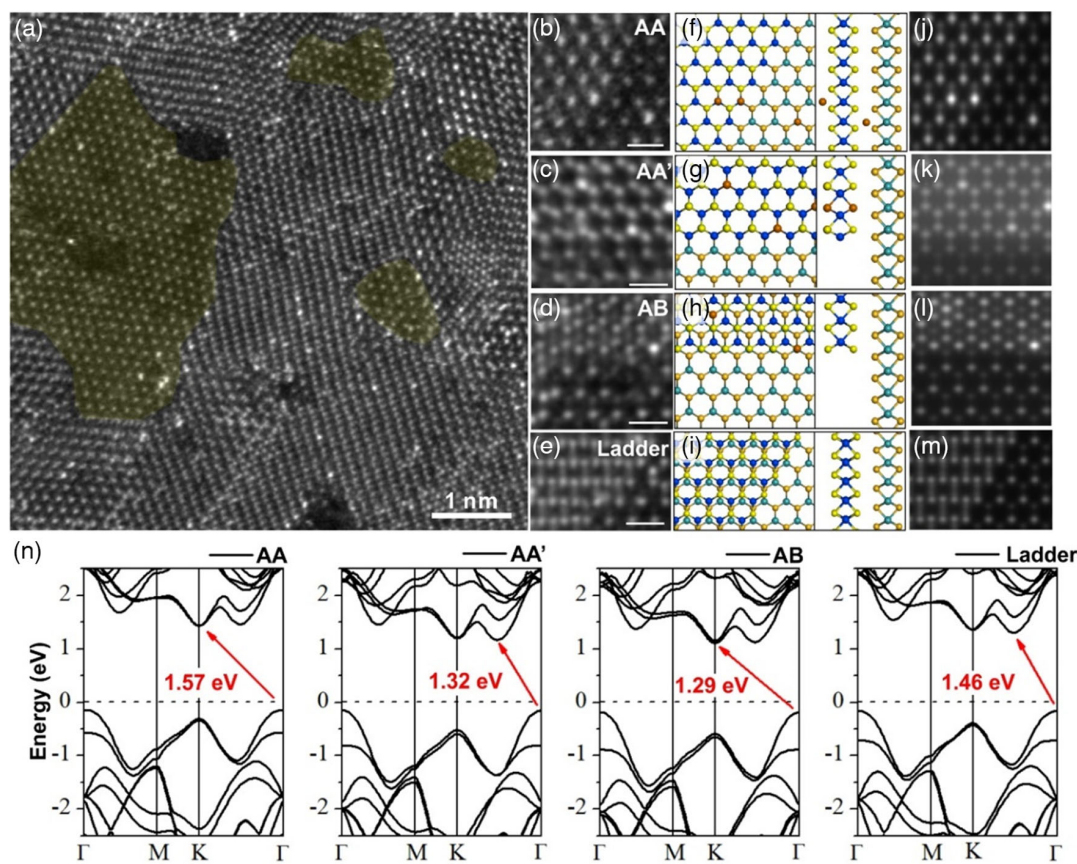


Figure 7. a) ADF-STEM image showing the atomic configuration of the bilayer $\text{MoS}_2\text{Te}_{2(1-x)}$ alloy. Yellow-shaded regions are monolayers, and the rest areas are bilayers. b–e) ADF-STEM images showing four typical kinds of interlayer stacking manners in the bilayer alloy. f–i) Atomic models corresponding to panels (b–e) showing both projection and side views. j–m) Multislice ADF-STEM simulation images corresponding to the models in panels (f–i). n) Band structure of bilayer 2H- MoS_2 with interlayer atomic registries of AA, AB, AA', and ladder, respectively.

AB, and ladder-like structures, most of which are inherited from the nomenclature of bilayer MoS_2 .^[60] The intralayer structure of all these bilayer stackings is the 2H-phase monolayer with hexagonal lattice. Detailed analysis of the four stacking orders is included in the supporting information (Figure S6a–d, Supporting Information).

DFT calculations were conducted to investigate whether the polytypism in bilayers would severely impact the electronic band structures locally. Considering the low Te concentration in the bilayer region and the calculation simplicity, we conducted DFT calculations on MoS_2 bilayers with different stacking manners to estimate the influence of the interlayer stacking on the band structure of the bilayer $\text{MoS}_{2x}\text{Te}_{2(1-x)}$ alloy. Figure 7n shows that different stacking orders exhibit varying indirect bandgaps ranging from 1.29 to 1.57 eV, showing slight energy discrepancy within 0.28 eV. The interlayer stacking variation predominantly alters the location of the conduction band minimum. When the spin-orbit coupling (SOC) effect is considered, the bandgaps are almost unchanged but the nondegenerate band numbers of AA- and AB-stacking have doubled because of the missing of inversion symmetry, which partly removes the Kramers' degeneracy compared with the AA' stacking and ladder stacking (Figure S6e, Supporting Information).

2.3. Structural Evolution of Monolayer 1T'- MoTe_2 in Oxygen Atmosphere and the Encapsulation Strategy

Finally, we investigated the detrimental composition and configuration change of 1T'- MoTe_2 by uncontrollably alloying with oxygen in air at room temperature. As shown in Figure 8a–c, the optical contrast of the 1T'- MoTe_2 domain, which reflects the material permittivity, quickly faded within 20 min, indicating the occurrence of oxidation. The atomic force microscopy (AFM) image of monolayer samples exposed in air exhibited a rough surface with discrete particles, suggesting the degradation of the 2D structural integrity when reacted with O (Figure S7, Supporting Information). The XPS spectrum of Te $3d_{5/2}$ and Te $3d_{3/2}$ corresponding to the aged specimen displays prominent signals situated at 576.2 and 586.5 eV, respectively, which correspond to Te–O bonds, manifesting the incorporation of element O in 1T'- MoTe_2 (Figure 8g).^[13] The presence of weak oxidized Te–O bands in the as-grown sample is due to an unavoidable short exposure time to air before and during the measurement. Characteristic Raman vibrational modes for 1T'- MoTe_2 are largely diminished for unprotected samples after exposure in air for 1 h (red curve in Figure 8h). These phenomena agree well with Te-based TMD atomic layers either exfoliated or CVD

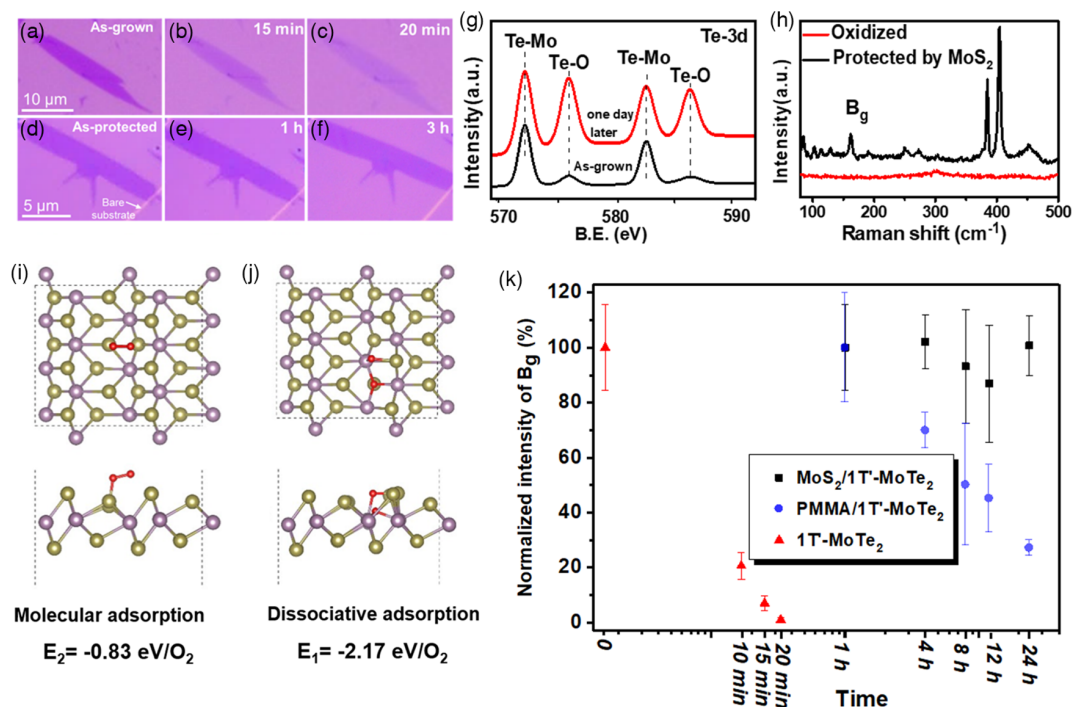


Figure 8. a–c) Optical images showing the structural evolution of monolayer 1T'-MoTe₂ exposed in air within 20 min. d–f) Optical images displaying the preservation of monolayer 1T'-MoTe₂ encapsulated by CVD-grown monolayer MoS₂ within 3 h. The scratch on the bottom right shows the contrast of the bare SiO₂/Si substrate, proving the existence of a uniform layer of MoS₂ on top of 1T'-MoTe₂. g) XPS spectra of Te 3d_{5/2} and 3d_{3/2} measured from fresh monolayer 1T'-MoTe₂ (black line) and the sample exposed in air for one day (red line), respectively. h) Raman spectra of nonprotected and MoS₂-encapsulated 1T' MoTe₂ samples, respectively, both after exposing to the ambient environment for 1 h. i, j) DFT-calculated structural evolution and the adsorption energy of monolayer 1T'-MoTe₂ with dissociative and molecular adsorption of O₂, respectively. Both the projective and the side views of the atomic models are given. Pink, yellow, and red spheres represent Mo, Te, and O atoms, respectively. k) Plot showing the intensity degradation of the normalized B_g peak in 1T'-MoTe₂ Raman spectra corresponding to exposed, PMMA-encapsulated, and MoS₂-encapsulated monolayer 1T'-MoTe₂, respectively.

prepared in the previous experimental reports,^[14,34,62–64] confirming universal vulnerability of this type of 2D material in oxygen atmosphere.

The possible degradation mechanism and the atomic structural evolution of 1T'-MoTe₂ were studied by DFT calculations. Figure 8i,j shows two potential paths. One is the molecular adsorption of O₂ on 1T'-MoTe₂, and the other is the dissociative adsorption of O₂. The molecular adsorption process is slightly exothermic ($E = -0.83$ eV/O₂), showing that an oxygen molecule binds on top of the Te site. In contrast, the dissociative adsorption energy of O₂ with 1T'-MoTe₂ is -2.17 eV/O₂, which is highly exothermic. Two dissociative oxygen atoms reside atop a Mo and a Te atom, respectively, and are bridged between two adjacent Mo and Te atoms. It can be seen that the dissociative adsorption of O₂ is remarkably favored over the molecular adsorption and is expected to result in fast and spontaneous oxidation of 1T'-MoTe₂ in ambient condition. These results well explain the high susceptibility of atomically thin 1T'-MoTe₂ in the presence of oxygen.

Given the high reactivity of 1T'-MoTe₂ in O-contained environment that severely hinders material's characterization and application, we developed a novel encapsulation method, which is swift, scalable, and enables the protection of 1T'-MoTe₂ and the fabrication of TMD vertical heterostructures at the same

time. This semidry transfer method used large-area monolayer MoS₂ grown by CVD as the coating layer (Figure S8, Supporting Information), which is distinctive from many other methods applying either exfoliated or CVD-grown multilayer 2D materials for insulation (see Experimental Section). Figure 8d–f shows the optical images of monolayer 1T'-MoTe₂ encapsulated by monolayer MoS₂. The contrast of 1T'-MoTe₂ is well maintained in 3 h, in sharp contrast with the scenario of the unprotected specimen. The Raman spectrum of MoS₂-encapsulated 1T'-MoTe₂ measured after 1 h exhibited characteristic peaks of both monolayer 1T'-MoTe₂ and MoS₂ (black curve in Figure 8h). These results demonstrate that the oxidation process of 1T'-MoTe₂ was effectively slowed down by single-layer MoS₂ passivation.

We monitored the antioxidation effect of the MoS₂ insulating layer over time and compared its performance with the widely used polymer membrane of poly (methyl methacrylate) (PMMA) (Figure 8k). The quantitative analysis was conducted by tracking the B_g peak intensity, which is the most prominent vibrational mode locating at ≈ 162 cm⁻¹ in 1T'-MoTe₂ and has been normalized with respect to the Si peak for each sample.^[34,42,65,66] It was found that the B_g intensity of unprotected 1T'-MoTe₂ monolayers drastically reduced by 80% in 10 min and became undetectable after 20 min. In

comparison, the B_g intensity was well maintained within 24 h for $1T'$ - MoTe_2 passivated by MoS_2 (Figure S9a, Supporting Information). Interestingly, the PMMA coating was incapable of effectively prohibiting the oxidation of $1T'$ - MoTe_2 , as the peak intensity reduced by 70% after 24 h (Figure S9b, Supporting Information). It may be ascribed to 1) the involvement of O-contained functional groups in the polymer chains that can slowly oxidize $1T'$ - MoTe_2 and 2) the inferior quality of the $1T'$ - MoTe_2 /PMMA interface that embedded air bubbles and cavities during the spin-coating process due to the absence of the atomic flatness of polymer films compared with the layered 2D materials like MoS_2 . These results verify the feasibility of isolating highly reactive $1T'$ - MoTe_2 from oxygen to avoid the uncontrollable alloying process by CVD-prepared single-layer MoS_2 and show its advantageous over polymer materials. It also provides a strategy to fabricate air-stable 2D MoS_2 / $1T'$ - MoTe_2 vdW heterostructures for device applications.

3. Conclusion

To sum up, we developed a space-confined CVD approach for the batch production of large-area, homogeneous $1T'$ - MoTe_2 monolayers in ambient pressure. The high-quality growth can be attributed to the viscous-to-Knudsen flow-state transition in the confined gap, thus eliminating the negative impact of concentration nonuniformity of the precursor vapor. Aberration-corrected ADF-STEM and DFT calculations were combined to unveil the structural evolution of atomically thin $1T'$ - MoTe_2 after alloying with sulfur and oxygen down to single-atom level. The sulfurization process led to $1T'$ -to-2H phase transition in MoTe_2 . Te atoms were found to situate not only at chalcogen sites but also at Mo sites in the $2\text{H-MoS}_{2x}\text{Te}_{2(1-x)}$ alloy. Both intralayer reconstruction and interlayer atomic registries were examined. Moreover, the atomic distribution of S and Te atoms in monolayer $\text{MoS}_{2x}\text{Te}_{2(1-x)}$ alloy was carefully investigated, showing the formation of homophilic and random configurations alloyed at 250 and 650 °C, respectively, indicating the potential of tailoring the alloying degree of different elements by temperature. Finally, the degradation of $1T'$ - MoTe_2 by the detrimental alloying process with oxygen in air was effectively suppressed by our newly developed encapsulation strategy via the CVD-prepared single-layer MoS_2 . DFT calculations were incorporated to predict the potential oxidation mechanism, as well as help understand the phase transition in the sulfurization process from the perspective of energy. These results give fundamental insights into both the beneficial (sulfurization) and the detrimental (oxidation) alloying process of $1T'$ - MoTe_2 monolayers with chalcogen elements. They also provide new ideas of tailoring the structure of 2D alloys via tuning the atomic distribution of different elements, which is an addition to the current ideas of the composition adjustment, Janus configuration construction, and the high-entropy alloy synthesis.

4. Experimental Section

Synthesis of Atomically Thin $1T'$ - MoTe_2 : The growth of $1T'$ - MoTe_2 monolayers was performed with a space-confined CVD system. First, the Si substrate with a 280 nm layer of SiO_2 (SiO_2/Si) was treated by oxygen plasma

for 2 min to make the surface more hydrophilic. The mixed solution of 0.03 M sodium molybdate (Na_2MoO_4 , 99%, Aladdin) and 0.1 M sodium chloride (NaCl , 99.9%, Aladdin) was subsequently spin coated on the substrate. The treated substrate was served as the bottom chip with another bare SiO_2/Si placed on top of it to generate a laminated substrate pair. The confined gap size between the two substrates could be adjusted by inserting mica sheets to increase the gap size or loading the quartz blocks on top of the substrate to decrease the gap size. Five pairs of vertically stacked substrates were loaded at the downstream of the 1 inch quartz tube. 80 mg of tellurium powder (Te, 99.99%, Aladdin) was put in a small ceramic boat at the upstream of the furnace, where the heating temperature was ≈ 450 °C during the synthesis. Before $1T'$ - MoTe_2 synthesis, the CVD system was flushed with the argon (Ar) gas flow of ≈ 500 sccm for 10 min to remove the air from the tube. Te powder was then preheated to provide sufficient Te vapor to the reaction zone. The furnace was heated to 750 °C with a heating rate of 20 °C min^{-1} under the Ar gas flow of 10 sccm and held for 5 min under the mixed gas of H_2/Ar at a flow rate of 40–70 sccm. The stacked substrate pairs were pushed into the central region of the furnace at this moment quickly and stayed for 30 min. Finally, the synthesis was stopped by a high flow rate of Ar gas flush and fast cooling of the furnace.

Alloying Process: Sulfurization of monolayer $1T'$ - MoTe_2 and tellurization of monolayer MoS_2 were conducted using a double-temperature zone furnace, in which the precise temperature of the chalcogen feedstocks and the substrate could be controlled independently. To obtain sulfurized $1T'$ - MoTe_2 , the fresh $1T'$ - MoTe_2 and 200 mg of sulfur (S) powder were loaded into the center of the two temperature zones, followed by flushing the tube with 500 sccm of ultrahigh-purity Ar gas for 10 min. During the sulfurization experiment, the temperatures of the S powder and the substrate were fixed at 200 and 250 °C, respectively, for 5 min. The sulfurization process was carried out at atmospheric pressure with 150 sccm of Ar gas, followed by fast cooling down to room temperature. For tellurization of monolayer MoS_2 , MoS_2 and 200 mg of Te powder were heated to 650 and 500 °C, respectively, with an Ar gas flow rate of 150 sccm. The synthesis was kept for 10 min.

Encapsulation of $1T'$ - MoTe_2 by the CVD-Grown Monolayer MoS_2 : The CVD synthesis of monolayer MoS_2 was reported in the previous work.^[67] Prior to the encapsulation of $1T'$ - MoTe_2 , the CVD-grown monolayer MoS_2 was transferred onto the flexible polydimethylsiloxane (PDMS, Aladdin) by a PMMA-etching-free method. As the surface energy was different between the hydrophobic MoS_2 and hydrophilic NaCl-modified SiO_2 , water spontaneously penetrated into the MoS_2 /substrate interface to delaminate MoS_2 . Specifically, as one droplet of deionized water was dropped on the corner of the growth substrate and gradually spread out on it, the MoS_2 sheet mildly detached. When all the monolayer MoS_2 floated on top of the water droplet, the PDMS held by self-closing tweezers was contacted gently to the droplet surface. After transferring MoS_2 to PDMS, the MoS_2 /PDMS assembly was baked under infrared light for 10 min to remove water residues. The transferred assembly was then stamped onto the fresh $1T'$ - MoTe_2 under an appropriate pressure. Once the encapsulation was completed, PDMS was peeled off by fine-tipped tweezers. It is worth noting that a rapid and effective encapsulation method right after the growth was necessary to stabilize the thin $1T'$ - MoTe_2 . The use of a thick and dry PDMS frame allows safely bringing MoS_2 right next to the reactor in which MoTe_2 was grown, so that the exposure of $1T'$ - MoTe_2 to air was limited to the few seconds necessary to unload the sample followed by a fully dry, top-down encapsulation of MoS_2 , minimizing its degradation before encapsulation.

Scanning Transmission Electron Microscopy and Image Processing: ADF-STEM imaging was conducted at room temperature on an aberration-corrected Titan Cubed Themis G2 300. STEM was operated under an accelerating voltage of 300 kV. Conditions were a condenser lens aperture of 50 mm, convergence semiangle of 21.3 mrad, and collection angle of 39–200 mrad. Dwell time of a single frame was 2 μs per pixel. A pixel size of 0.012 nm px^{-1} , as well as a beam current of 30 pA, was used for imaging. Images were processed using ImageJ software. A Gaussian blur filter (≈ 2 –4 pixels) was used on high-magnification ADF-STEM images for smoothing. A fire or orange hot false color lookup table

was applied to some grayscale ADF–STEM images to improve the visualization. Atomic models were constructed using the software of Accelrys Discovery Studio Visualizer. ADF–STEM image simulations based on corresponding atomic models were generated using COMPUTEM software with proper parameter adjustment in light of the imaging conditions.

Calculation Methods: All first-principles calculations based on the DFT were implemented in the Vienna Ab-initio Simulation Package (VASP).^[68,69] We used generalized gradient approximation (GGA) in the Perdew–Burke–Ernzerhof formalism for describing the exchange–correlation functional, using the projector-augmented wave (PAW) method to treat the core electrons, with a cutoff energy of 600 eV in the planewave basis to describe electron wavefunction and a $16 \times 16 \times 1$ Γ -centered Monkhorst–Pack grid to sample the 2D Brillouin zone.^[70,71] A vacuum layer larger than 15 Å along the *c*-axis was used to screen the interaction between neighbor repeated images. In bilayer systems, vdW correction given by the DFT-D3 method was used to treat the interlayer vdW interactions,^[72] and dipole correction was used to correct the potential errors in aperiodic *c*-direction. In structural optimization, the energy convergence criterion was set as 10^{-7} eV f.u.⁻¹ and the tolerance of the Hellmann–Feynman forces was set as 0.01 eV Å⁻¹.

Supporting Information

Supporting Information is available from the Wiley Online Library or from the author.

Acknowledgements

S.W. acknowledges support from the National Natural Science Foundation of China (52172032 and 21805305), State Administration of Science, Technology and Industry for National Defense (WDZC20195500503), National University of Defense Technology (ZK18-01-03 and ZZKY-YX-09-01), and Young Talents Support Project from China Association for Science and Technology (no. YESS20200222). J.Z. acknowledges financial support from the Ministry of Science and Technology of China (2016YFA0200100 and 2018YFA0703502), the National Natural Science Foundation of China (grant nos. 52021006, 51720105003, 21790052, and 21974004), the Strategic Priority Research Program of CAS (XDB36030100), and the Beijing National Laboratory for Molecular Sciences (BNLMS-CXTD-202001). This work was carried out in part using computing resources at the High Performance Computing Center of Central South University. O.F. acknowledges the National Natural Science Foundation of China (grant no. 52073308).

Conflict of Interest

The authors declare no conflict of interest.

Author Contributions

T.X., S.L., and A.L. contributed equally to this work. S.W. and J.Z. initiated the project and generated the experimental protocols. T.X. conducted the chemical vapor deposition growth of atomically thin 1T'-MoTe₂. S.L. synthesized the 2D MoS₂xTe₂(1-x) alloy. Y.Y. and S.W. performed the annular dark field scanning transmission electron microscopy (ADF–STEM) characterization of the specimen. O.L. and O.F. performed Density functional theory calculations. All authors contributed to data processing, result discussion, as well as the writing and revision of the manuscript.

Data Availability Statement

Research data are not shared.

Keywords

1T'-MoTe₂, 2D alloys, ADF-STEM, density functional theory, transition metal dichalcogenides

Received: February 8, 2022

Revised: May 19, 2022

Published online: June 22, 2022

- [1] E. P. George, D. Raabe, R. O. Ritchie, *Nat. Rev. Mater.* **2019**, *4*, 515.
- [2] L. Pavesi, M. Guzzi, *J. Appl. Phys.* **1994**, *75*, 4779.
- [3] K. P. O'Donnell, I. Fernandez-Torrente, P. R. Edwards, R. W. Martin, *J. Cryst. Growth* **2004**, *269*, 100.
- [4] M. Basharat, M. A. Hannan, N. A. Shah, A. Ali, M. Arif, A. Maqsood, *Cryst. Res. Technol.* **2007**, *42*, 817.
- [5] X. Liu, J. Wu, W. Yu, L. Chen, Z. Huang, H. Jiang, J. He, Q. Liu, Y. Lu, D. Zhu, W. Liu, P. Cao, S. Han, X. Xiong, W. Xu, J. P. Ao, K. W. Ang, Z. He, *Adv. Funct. Mater.* **2017**, *27*, 1606469.
- [6] W. Wen, Y. Zhu, X. Liu, H. P. Hsu, Z. Fei, Y. Chen, X. Wang, M. Zhang, K. H. Lin, F. S. Huang, Y. P. Wang, Y. S. Huang, C. H. Ho, P. H. Tan, C. Jin, L. Xie, *Small* **2017**, *13*, 1603788.
- [7] Z. Hemmat, J. Cavin, A. Ahmadiparidari, A. Ruckel, S. Rastegar, S. N. Misal, L. Majidi, K. Kumar, S. Wang, J. Guo, R. Dawood, F. Lagunas, P. Parajuli, A. T. Ngo, L. A. Curtiss, S. B. Cho, J. Cabana, R. F. Klie, R. Mishra, A. Salehi-Khojin, *Adv. Mater.* **2020**, *32*, 1907041.
- [8] Q. Fu, L. Yang, W. Wang, A. Han, J. Huang, P. Du, Z. Fan, J. Zhang, B. Xiang, *Adv. Mater.* **2015**, *27*, 4732.
- [9] S. Wang, A. Robertson, J. H. Warner, *Chem. Soc. Rev.* **2018**, *47*, 6764.
- [10] M. Zeng, Y. Xiao, J. Liu, K. Yang, L. Fu, *Chem. Rev.* **2018**, *118*, 6236.
- [11] J. Zhou, J. Lin, X. Huang, Y. Zhou, Y. Chen, J. Xia, H. Wang, Y. Xie, H. Yu, J. Lei, D. Wu, F. Liu, Q. Fu, Q. Zeng, C. H. Hsu, C. Yang, L. Lu, T. Yu, Z. Shen, H. Lin, B. I. Yakobson, Q. Liu, K. Suenaga, G. Liu, Z. Liu, *Nature* **2018**, *556*, 355.
- [12] S. Wang, Z. Qin, G. S. Jung, F. J. Martin-Martinez, K. Zhang, M. J. Buehler, J. H. Warner, *ACS Nano* **2016**, *10*, 9831.
- [13] L. Ma, J. Zhu, W. Li, R. Huang, X. Wang, J. Guo, J. H. Choi, Y. Lou, D. Wang, G. Zou, *J. Am. Chem. Soc.* **2021**, *143*, 13314.
- [14] X. Xu, Y. Pan, S. Liu, B. Han, P. Gu, S. Li, W. Xu, Y. Peng, Z. Han, J. Chen, P. Gao, Y. Ye, *Science* **2021**, *372*, 195.
- [15] J. Zhang, S. Jia, I. Kholmanov, L. Dong, D. Er, W. Chen, H. Guo, Z. Jin, V. B. Shenoy, L. Shi, J. Lou, *ACS Nano* **2017**, *11*, 8192.
- [16] A. Y. Lu, H. Zhu, J. Xiao, C. P. Chuu, Y. Han, M. H. Chiu, C. C. Cheng, C. W. Yang, K. H. Wei, Y. Yang, Y. Wang, D. Sokaras, D. Nordlund, P. Yang, D. A. Muller, M. Y. Chou, X. Zhang, L. J. Li, *Nat. Nanotechnol.* **2017**, *12*, 744.
- [17] J. Cavin, A. Ahmadiparidari, L. Majidi, A. S. Thind, S. N. Misal, A. Prajapati, Z. Hemmat, S. Rastegar, A. Beukelman, M. R. Singh, K. A. Unocic, A. Salehi-Khojin, R. Mishra, *Adv. Mater.* **2021**, *33*, 2100347.
- [18] A. Apte, A. Krishnamoorthy, J. A. Hachtel, S. Susarla, J. C. Idrobo, A. Nakano, R. K. Kalia, P. Vashishta, C. S. Tiwary, P. M. Ajayan, *Chem. Mater.* **2018**, *30*, 7262.
- [19] Y. Gong, Z. Liu, A. R. Lupini, G. Shi, J. Lin, S. Najmaei, Z. Lin, A. Laura, A. Berkdemir, G. You, H. Terrones, M. Terrones, R. Vajtai, S. T. Pantelides, S. J. Pennycook, J. Lou, W. Zhou, P. M. Ajayan, *Nano Lett.* **2014**, *14*, 442.
- [20] Q. Feng, Y. Zhu, J. Hong, M. Zhang, W. Duan, N. Mao, J. Wu, H. Xu, F. Dong, F. Lin, C. Jin, C. Wang, J. Zhang, L. Xie, *Adv. Mater.* **2014**, *26*, 2648.
- [21] X. Duan, C. Wang, Z. Fan, G. Hao, L. Kou, U. Halim, H. Li, X. Wu, Y. Wang, J. Jiang, A. Pan, Y. Huang, R. Yu, X. Duan, *Nano Lett.* **2016**, *16*, 264.

- [22] S. Susarla, J. A. Hachtel, X. Yang, A. Kutana, A. Apte, Z. Jin, R. Vajtai, J. C. Idrobo, J. Lou, B. I. Yakobson, C. S. Tiwary, P. M. Ajayan, *Adv. Mater.* **2018**, *30*, 1804218.
- [23] H. Li, X. Duan, X. Wu, X. Zhuang, H. Zhou, Q. Zhang, X. Zhu, A. Pan, X. Duan, *J. Am. Chem. Soc.* **2014**, *136*, 3756.
- [24] P. Li, J. Cui, J. Zhou, D. Guo, Z. Zhao, J. Yi, J. Fan, Z. Ji, X. Jing, F. Qu, C. Yang, L. Lu, J. Lin, Z. Liu, G. Liu, *Adv. Mater.* **2019**, *31*, 1904641.
- [25] B. Tang, J. Zhou, P. Sun, X. Wang, L. Bai, J. Dan, J. Yang, K. Zhou, X. Zhao, S. J. Pennycook, Z. Liu, *Adv. Mater.* **2019**, *31*, 1900862.
- [26] P. Yu, J. Lin, L. Sun, Q. L. Le, X. Yu, G. Gao, C. H. Hsu, D. Wu, T. R. Chang, Q. Zeng, F. Liu, Q. J. Wang, H. T. Jeng, H. Lin, A. Trampert, Z. Shen, K. Suenaga, Z. Liu, *Adv. Mater.* **2017**, *29*, 1603991.
- [27] J. Lin, J. Zhou, S. Zuluaga, P. Yu, M. Gu, Z. Liu, S. T. Pantelides, K. Suenaga, *ACS Nano* **2018**, *12*, 894.
- [28] H. You, Z. Zhuo, X. Lu, Y. Liu, Y. Guo, W. Wang, H. Yang, X. Wu, H. Li, T. Zhai, *CCS Chem.* **2019**, *1*, 396.
- [29] G. Mirabelli, C. McGeough, M. Schmidt, E. K. McCarthy, S. Monaghan, I. M. Povey, M. McCarthy, F. Gity, R. Nagle, G. Hughes, A. Cafolla, P. K. Hurley, R. Duffy, *J. Appl. Phys.* **2016**, *120*, 125102.
- [30] G. Wang, R. Pandey, S. P. Karna, *Wiley Interdiscip. Rev.: Comput. Mol. Sci.* **2017**, *7*, e1280.
- [31] Q. Li, Q. Zhou, L. Shi, Q. Chen, J. Wang, *J. Mater. Chem. A* **2019**, *7*, 4291.
- [32] S. Eizagirre Barker, S. Wang, R. H. Godiksen, G. W. Castellanos, M. Berghuis, T. V. Raziman, A. G. Curto, J. Gómez Rivas, *Adv. Opt. Mater.* **2019**, *7*, 1900351.
- [33] R. Zan, Q. M. Ramasse, R. Jalil, T. Georgiou, U. Bangert, K. S. Novoselov, *ACS Nano* **2013**, *7*, 10167.
- [34] S. Pace, L. Martini, D. Convertino, D. H. Keum, S. Forti, S. Pezzini, F. Fabbri, V. Mišekis, C. Coletti, *ACS Nano* **2021**, *15*, 4213.
- [35] S. J. Yun, G. H. Han, H. Kim, D. L. Duong, B. G. Shin, J. Zhao, Q. A. Vu, J. Lee, S. M. Lee, Y. H. Lee, *Nat. Commun.* **2017**, *8*, 2163.
- [36] S. Zhou, L. Gan, D. Wang, H. Li, T. Zhai, *Nano Res.* **2018**, *11*, 2909.
- [37] X. Xu, Z. Zhang, L. Qiu, J. Zhuang, L. Zhang, H. Wang, C. Liao, H. Song, R. Qiao, P. Gao, Z. Hu, L. Liao, Z. Liao, D. Yu, E. Wang, F. Ding, H. Peng, K. Liu, *Nat. Nanotechnol.* **2016**, *11*, 930.
- [38] C. C. Chen, C. J. Kuo, C. Da Liao, C. F. Chang, C. A. Tseng, C. R. Liu, Y. T. Chen, *Chem. Mater.* **2015**, *27*, 6249.
- [39] S. Chen, H. Ji, H. Chou, Q. Li, H. Li, J. W. Suk, R. Piner, L. Liao, W. Cai, R. S. Ruoff, *Adv. Mater.* **2013**, *25*, 2062.
- [40] X. Li, C. W. Magnuson, A. Venugopal, R. M. Tromp, J. B. Hannon, E. M. Vogel, L. Colombo, R. S. Ruoff, R. S. Ruo, *J. Am. Chem. Soc.* **2011**, *133*, 2816.
- [41] L. Zhou, A. Zubair, Z. Wang, X. Zhang, F. Ouyang, K. Xu, W. Fang, K. Ueno, J. Li, T. Palacios, J. Kong, M. S. Dresselhaus, *Adv. Mater.* **2016**, *28*, 9526.
- [42] M. Kan, H. G. Nam, Y. H. Lee, Q. Sun, *Phys. Chem. Chem. Phys.* **2015**, *17*, 14866.
- [43] D. H. Keum, S. Cho, J. H. Kim, D. H. Choe, H. J. Sung, M. Kan, H. Kang, J. Y. Hwang, S. W. Kim, H. Yang, K. J. Chang, Y. H. Lee, *Nat. Phys.* **2015**, *11*, 482.
- [44] L. Sun, Z. Wang, Y. Wang, L. Zhao, Y. Li, B. Chen, S. Huang, S. Zhang, W. Wang, D. Pei, H. Fang, S. Zhong, H. Liu, J. Zhang, L. Tong, Y. Chen, Z. Li, M. H. Rummeli, K. S. Novoselov, H. Peng, L. Lin, Z. Liu, *Nat. Commun.* **2021**, *12*, 2391.
- [45] S. Wang, Y. Rong, Y. Fan, M. Pacios, H. Bhaskaran, K. He, J. H. Warner, *Chem. Mater.* **2014**, *26*, 6371.
- [46] H. Li, Q. Zhang, C. C. R. Yap, B. K. Tay, T. H. T. Edwin, A. Olivier, D. Baillargeat, *Adv. Funct. Mater.* **2012**, *22*, 1385.
- [47] A. T. Hoang, S. M. Shinde, A. K. Katiyar, K. P. Dhakal, X. Chen, H. Kim, S. W. Lee, Z. Lee, J. H. Ahn, *Nanoscale* **2018**, *10*, 21978.
- [48] C. Zhang, S. Kc, Y. Nie, C. Liang, W. G. Vandenberghe, R. C. Longo, Y. Zheng, F. Kong, S. Hong, R. M. Wallace, K. Cho, *ACS Nano* **2016**, *10*, 7370.
- [49] H. Taghinejad, D. A. Rehn, C. Muccianti, A. A. Eftekhar, M. Tian, T. Fan, X. Zhang, Y. Meng, Y. Chen, T. V. Nguyen, S. F. Shi, P. M. Ajayan, J. Schaiabley, E. J. Reed, A. Adibi, *ACS Nano* **2018**, *12*, 12795.
- [50] D. O. Dumcenco, H. Kobayashi, Z. Liu, Y.-S. Huang, K. Suenaga, *Nat. Commun.* **2013**, *4*, 1351.
- [51] B. J. Hwang, L. S. Sarma, J. M. Chen, C. H. Chen, S. C. Shin, Q. R. Wang, D. G. Liu, J. F. Lee, M. T. Tang, *J. Am. Chem. Soc.* **2005**, *127*, 11140.
- [52] M. Zhu, G. Sun, Q. Xin, *Electrochim. Acta* **2009**, *54*, 1511.
- [53] S. Wang, G. Do Lee, S. Lee, E. Yoon, J. H. Warner, *ACS Nano* **2016**, *10*, 5419.
- [54] H. Yoo, R. Engelke, S. Carr, S. Fang, K. Zhang, P. Cazeaux, S. H. Sung, R. Hovden, A. W. Tsen, T. Taniguchi, K. Watanabe, G. C. Yi, M. Kim, M. Lusk, E. B. Tadmor, E. Kaxiras, P. Kim, *Nat. Mater.* **2019**, *18*, 448.
- [55] P. C. Yeh, W. Jin, N. Zaki, J. Kunstmann, D. Chenet, G. Arefe, J. T. Sadowski, J. I. Dadap, P. Sutter, J. Hone, R. M. Osgood, *Nano Lett.* **2016**, *16*, 953.
- [56] M. Xia, B. Li, K. Yin, G. Capellini, G. Niu, Y. Gong, W. Zhou, P. M. Ajayan, Y. H. Xie, *ACS Nano* **2015**, *9*, 12246.
- [57] G. S. Jung, S. Wang, Z. Qin, F. J. Martin-Martinez, J. H. Warner, M. J. Buehler, *ACS Nano* **2018**, *12*, 3600.
- [58] S. Chen, M. He, Y. H. Zhang, V. Hsieh, Z. Fei, K. Watanabe, T. Taniguchi, D. H. Cobden, X. Xu, C. R. Dean, M. Yankowitz, *Nat. Phys.* **2021**, *17*, 374.
- [59] X. Zhao, W. Sun, D. Geng, W. Fu, J. Dan, Y. Xie, P. R. C. Kent, W. Zhou, S. J. Pennycook, K. P. Loh, *Adv. Mater.* **2019**, *31*, 1808343.
- [60] S. Wang, H. Sawada, C. S. Allen, A. I. Kirkland, J. H. Warner, *Nanoscale* **2017**, *9*, 13060.
- [61] S. Wang, Y. Yu, S. Zhang, S. Zhang, H. Xu, X. Zou, J. Zhang, *Matter* **2020**, *3*, 2108.
- [62] W. Yu, Z. Dong, I. Abdelwahab, X. Zhao, J. Shi, Y. Shao, J. Li, X. Hu, *ACS Nano* **2021**, *15*, 18448.
- [63] X. Zheng, Y. Wei, C. Deng, H. Huang, Y. Yu, G. Wang, G. Peng, Z. Zhu, Y. Zhang, T. Jiang, S. Qin, R. Zhang, X. Zhang, *ACS Appl. Mater. Interfaces* **2018**, *10*, 30045.
- [64] S. H. Yang, C. Y. Lin, Y. M. Chang, M. Li, K. C. Lee, C. F. Chen, F. S. Yang, C. H. Lien, K. Ueno, K. Watanabe, T. Taniguchi, K. Tsukagoshi, Y. F. Lin, *ACS Appl. Mater. Interfaces* **2019**, *11*, 47047.
- [65] T. A. Empante, Y. Zhou, V. Klee, A. E. Nguyen, I. H. Lu, M. D. Valentin, S. A. Naghbi Al Villar, E. Preciado, A. J. Berges, C. S. Merida, M. Gomez, S. Bobek, M. Isarraraz, E. J. Reed, L. Bartels, *ACS Nano* **2017**, *11*, 900.
- [66] R. S. Lee, D. Kim, S. A. Pawar, T. Kim, J. C. Shin, S. Kang, *ACS Nano* **2019**, *13*, 642.
- [67] S. Li, S. Wang, T. Xu, H. Zhang, Y. Tang, S. Liu, T. Jiang, S. Zhou, H. Cheng, *Nanoscale* **2021**, *13*, 13030.
- [68] R. A. Vargas-Hernández, *J. Phys. Chem. A* **2020**, *124*, 4053.
- [69] G. Kresse, J. Furthmüller, *Comput. Mater. Sci.* **1996**, *6*, 15.
- [70] J. P. Perdew, K. Burke, M. Ernzerhof, *Phys. Rev. Lett.* **1996**, *77*, 3865.
- [71] P. E. Blöchl, *Phys. Rev. B* **1994**, *50*, 17953.
- [72] S. Grimme, J. Antony, S. Ehrlich, H. Krieg, *J. Chem. Phys.* **2010**, *132*, 154104.